ADVANCED FUNCTIONAL MATERIALS
www.afm-journal.de

Lithium Phosphonate Functionalized Polymer Coating for High-Energy $Li[Ni_{0.8}Co_{0.1}Mn_{0.1}]O_2$ with Superior Performance at Ambient and Elevated Temperatures

Zhen Chen, Huu-Dat Nguyen, Maider Zarrabeitia, Hai-Peng Liang, Dorin Geiger, Jae-Kwang Kim, Ute Kaiser, Stefano Passerini, Cristina Iojoiu,* and Dominic Bresser**

High-energy Ni-rich lithium transition metal oxides such as $Li[Ni_{0.8}Co_{0.1}Mn_{0.1}]O_2$ (NCM_{811}) are appealing positive electrode materials for next-generation lithium batteries. However, the high sensitivity toward moist air during storage and the high reactivity with common organic electrolytes, especially at elevated temperatures, are hindering their commercial use. Herein, an effective strategy is reported to overcome these issues by coating the NCM_{811} particles with a lithium phosphonate functionalized poly(aryl ether sulfone). The application of this coating allows for a substantial reduction of lithium-based surface impurities (e.g., LiOH, Li_2CO_3) and, generally, the suppression of detrimental side reactions upon both storage and cycling. As a result, the coated NCM_{811}-based cathodes reveal superior Coulombic efficiency and cycling stability at ambient and, particularly, at elevated temperatures up to 60 °C (a temperature at which the non-coated NCM_{811} electrodes rapidly fail) owing to the formation of a stable cathode electrolyte interphase with enhanced Li^+ transport kinetics and the well-retained layered crystal structure. These results render the herein presented coating strategy generally applicable for high-performance lithium battery cathodes.

1. Introduction

Ni-rich $LiNi_{1-x-y}Co_xMn_yO_2$ ($NCM_{(1-x-y)xy}$, with $1-x-y \geq 0.6$) cathode materials are considered the most practical candidates for high-energy lithium-ion and lithium-metal batteries owing to their high capacities and good rate capability.[1] However, there are several challenges that remain to be overcome for a widespread use in commercial battery cells:[2] 1) the difficulty in synthesizing stoichiometric NCM due to the instability of trivalent nickel during the high-temperature calcination process;[2a] 2) the high sensitivity toward moist air and facile formation of surface impurities (e.g., LiOH, Li_2CO_3), causing inferior cycling stability;[3] 3) the Li^+/Ni^{2+} cation mixing, leading to severe structural changes;[4] and 4) the inferior thermal stability with an increasing nickel content, raising serious safety concerns. In fact, the higher the nickel content, the more pronounced are the abovementioned challenges and the more effective need to be the strategies to overcome these, especially for Ni-rich $NCM_{(1-x-y)xy}$ with $1-x-y \geq 0.8$.[5] According to Ryu et al.[6] an abrupt anisotropic shrinkage caused by phase transitions toward the end of charge occurs when the Ni content exceeds 0.8. This stress-inducing volume shrinkage and subsequent expansion initiates the propagation of microcracks from the bulk to the surface, leading to progressive capacity decay upon cycling. Moreover, such high nickel contents lead to an increasingly pronounced reactivity with moist air, requiring a consequent storage, handling, and processing under very dry or inert atmosphere – not least as the otherwise formed LiOH, Li_2CO_3, and transition metal carbonates (TM_xCO_3)[7] cause the gelation of the slurry during the electrode preparation due to the pH increase,[8] exacerbate gas evolution at elevated potentials (along with the oxygen release

Dr. Z. Chen, Dr. M. Zarrabeitia, H.-P. Liang, Prof. S. Passerini, Dr. D. Bresser
Helmholtz Institute Ulm (HIU)
89081 Ulm, Germany
E-mail: stefano.passerini@kit.edu; dominic.bresser@kit.edu
Dr. Z. Chen, Dr. M. Zarrabeitia, H.-P. Liang, Prof. S. Passerini, Dr. D. Bresser
Karlsruhe Institute of Technology (KIT)
76021 Karlsruhe, Germany
The ORCID identification number(s) for the author(s) of this article can be found under https://doi.org/10.1002/adfm.202105343.

© 2021 The Authors. Advanced Functional Materials published by Wiley-VCH GmbH. This is an open access article under the terms of the Creative Commons Attribution License, which permits use, distribution and reproduction in any medium, provided the original work is properly cited.

DOI: 10.1002/adfm.202105343

Dr. H.-D. Nguyen, Dr. C. Iojoiu
Univ. Grenoble Alpes
Univ. Savoie Mont Blanc
CNRS, Grenoble INP, LEPMI, Grenoble 38 000, France
E-mail: cristina.iojoiu@lepmi.grenoble-inp.fr
Dr. H.-D. Nguyen, Dr. C. Iojoiu
Réseau sur le Stockage Electrochimique de l'Energie (RS2E)
CNRS, FR3459, Amiens, Cedex 80 039, France
Dr. D. Geiger, Prof. U. Kaiser
Central Facility of Electron Microscopy
Electron Microscopy Group of Materials Science
Ulm University
Albert-Einstein-Allee 11, D-89081 Ulm, Germany
Prof. J.-K. Kim
Department of Solar & Energy Engineering
Cheongju University
Cheongju, Chungbuk 28503, Republic of Korea

resulting from the layered to spinel and rock-salt structural transition),[9] and thus eventually have a detrimental impact on the cycling stability and capacity retention.

To address these challenges, various approaches have been adopted, including advanced material and particle designs such as the realization of core–shell structures[10] and transition metal concentration gradients,[11] the incorporation of functional dopants,[12] and the application of inorganic or organic surface coatings, including metal oxides,[13] metal fluorides,[14] metal phosphates,[3,15] and polymers.[15b,16] The latter approach appears particularly straightforward, as such protective coatings can physically prevent the contact with the ambient atmosphere, while also stabilizing the interface with the electrolyte in the battery cell – especially with regard to the essentially unlimited choice of suitable coating compositions, allowing for well-tailored properties. Nonetheless, the use of inorganic coatings commonly requires additional calcination steps at several hundred degrees Celsius, which leads to significantly higher cost and complicates recycling. In addition, lithium-free coating layers (inorganic or organic) hinder Li^+ transport across the interface with the electrolyte, particularly when surpassing a certain thickness, which negatively affects the cell performance at elevated current densities.[17]

Herein, we report lithium phosphonate functionalized poly(arylene ether sulfone) (PP10-Li; see **Figure 1**a) as suitable coating layer for high-energy NCM_{811} ($ONCM_{811}$) to overcome the aforementioned challenges. The beneficial interaction with the NCM_{811} particles allows for a highly homogeneous coating at room temperature, while the lithium phosphonate function facilitates charge transfer and the poly(arylene)-type backbone enhances the thermal stability and thus safety of the cathode material. Advantageously, the application of the PP10-Li coating moreover leads to a substantially reduced amount of detrimental surface impurities such as LiOH and Li_2CO_3 and, instead, an enrichment in LiF at the active material surface. As a result, $ONCM_{811}$ shows superior rate capability and enhanced cycling stability, especially at elevated temperatures up to 60 °C compared to the non-coated NCM_{811}.

2. Results and Discussion

2.1. Physicochemical Characterization

In a first step, we investigated the morphology of the PP10-Li coating. Figure 1b shows a scanning electron microscopy (SEM) image of the NCM_{811} active material, containing secondary particles with a diameter of either ≈2 µm or ≈15 µm to increase the electrode packing density and thus the energy density eventually. This particle morphology is well preserved after applying the PP10-Li coating, as depicted in Figure 1c. The only difference at this magnification appears to be the observation of some darker spots, which are assigned to the electronically insulating nature of PP10-Li, uniformly covering the NCM_{811} particle surface as apparent at higher magnification (Figure 1d). Transmission electron microscopy (TEM) images of NCM_{811} confirm the secondary particle structure (Figure 1e) and high-resolution TEM analysis of the particles (Figure 1f) reveals clear lattice fringes assigned to the (003) plane of the layered crystal structure, indicating that the material is highly crystalline (see also the fast Fourier transform (FFT) pattern in the inset), which is in good agreement with results obtained by X-ray diffraction (XRD), presented in Figure S1 (Supporting Information). In fact, in both cases – NCM_{811} and $ONCM_{811}$ – the same reflections are observed, which can be well assigned to the layered α-$NaFeO_2$ structure (R–3m) and there is no indication of any phase impurity for neither of the two materials. The TEM analysis of the $ONCM_{811}$ reveals that the PP10-Li coating layer has a rather homogeneous thickness of 7–12 nm and uniformly covers the particle surface (Figure 1g), which is well in line with the SEM data (Figure 1d). To further confirm the uniformity of the coating, we conducted energy-dispersive X-ray (EDX) spectroscopy mappings of a larger secondary $ONCM_{811}$ particle (Figure 1h) and an extendedly larger region of pristine $ONCM_{811}$-based electrodes (Figure S2, Supporting Information); and, indeed, the mappings of the different elements (Figure 1i–p and Figure S2b-i: Supporting Information) – especially sulfur and phosphorus (Figure 1k,l and Figure S2d,e: Supporting Information), which are present only in PP10-Li – reveals a very homogeneous distribution at the particle surface.

In a next step, we performed a comparative investigation of pristine NCM_{811} and $ONCM_{811}$ electrodes via X-ray photoelectron spectroscopy (XPS) to study the impact of applying the PP10-Li coating on the surface chemistry. A summary of the findings for the oxygen-containing species is provided in **Figure 2**a (based on the fitting of the O 1s spectra shown in Figure S3, Supporting Information). The intensity of the M-O contribution (in purple) is noticeably lower in the case of $ONCM_{811}$ compared to NCM_{811} as a result of the PP10-Li coating. The presence of the coating is also reflected in the contributions from S = O (in dark purple) and O = POLi (in light purple) as well as the pronounced contribution of -COC- (in orange). The presence of the latter contribution for the NCM_{811} spectrum, but to a substantially lower extent, is assigned to oxygen species at the surface of the conductive carbon. The minor contribution of R-O-(C = O)-O- as additional surface species, observed for both pristine NCM_{811} and $ONCM_{811}$ electrodes, originates from the reaction of the electrode material with the atmosphere.[18] Although all the material handling and processing as well as the electrode preparation were conducted in the dry room, the formation of surface contaminations such as LiOH and Li_2CO_3 owing to the reaction with the ambient atmosphere (especially, H_2O and CO_2) could not be fully suppressed. The contribution of LiOH is very low in the case of NCM_{811} (≈0.22 at%) owing to the careful handling in the glove box and dry room, while it is essentially undetectable for $ONCM_{811}$. Similarly, the contribution of Li_2CO_3 is much more pronounced for NCM_{811} (4.92 at%) compared to $ONCM_{811}$ (1.17 at%). The reduced contribution of LiOH and Li_2CO_3 observed for $ONCM_{811}$ highlights the substantially decreased reactivity with the ambient atmosphere, as a result of the homogeneous PP10-Li coating which effectively prevents the direct exposure to H_2O and CO_2.[19] This finding is of particular relevance with regard to the commercial use of Ni-rich NCM, since the formation of LiOH and Li_2CO_3 does not only cause lower specific capacities, but moreover leads to a higher interfacial resistance, pronounced side reactions with the electrolyte, and gas formation during cycling.[20]

© 2021 The Authors. Advanced Functional Materials published by Wiley-VCH GmbH

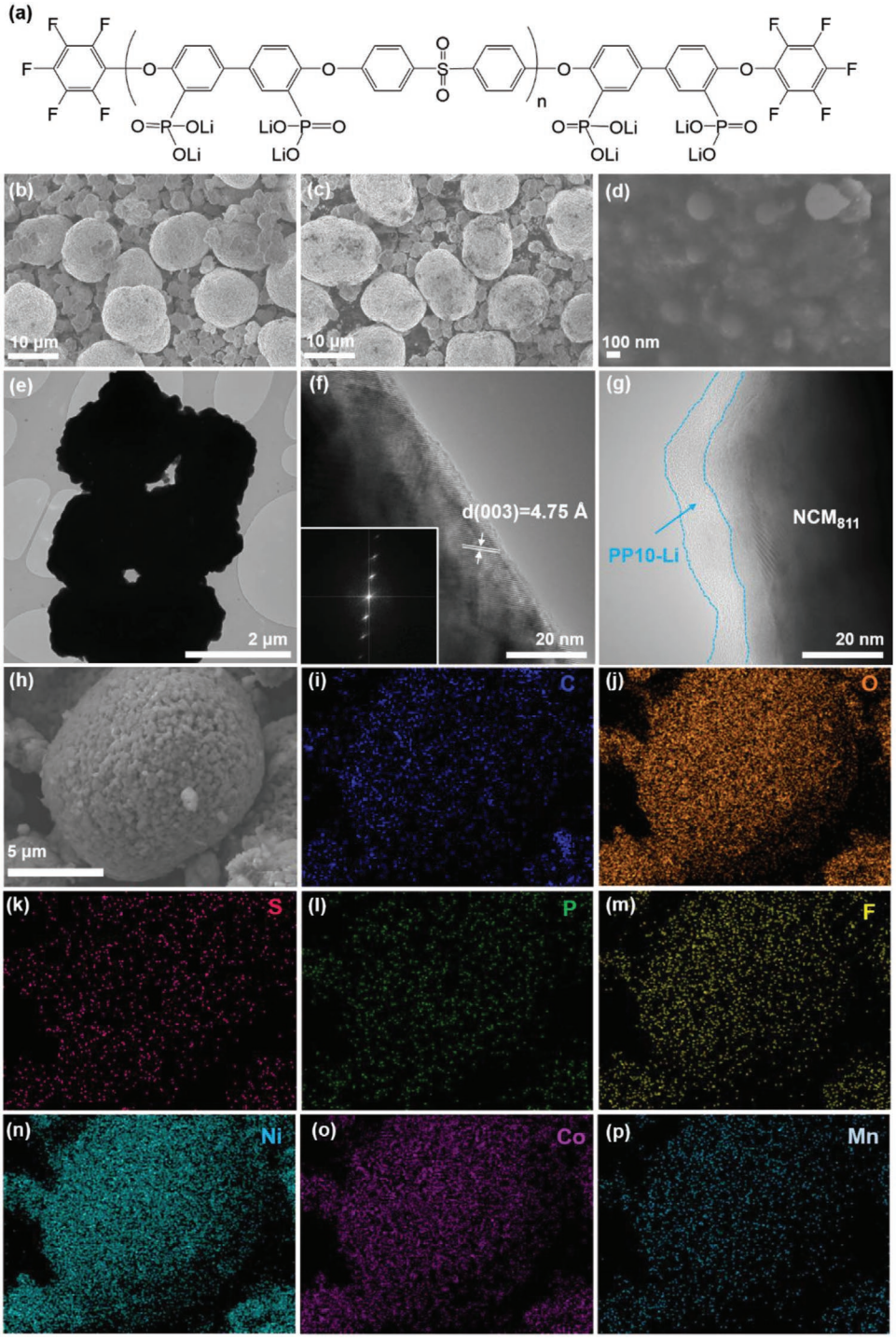

Figure 1. a) Chemical structure of the lithium phosphonate functionalized poly(arylene ether sulfone), herein referred to as PP10-Li. SEM images of b) NCM_{811} and c,d) $ONCM_{811}$ particles. TEM images of e,f) NCM_{811} (with the FFT pattern as inset in (f)) and g) $ONCM_{811}$ – the latter includes an indication of the PP10-Li layer with a rather homogeneous thickness of about 10 nm. h) SEM image of a secondary $ONCM_{811}$ particle that was studied via EDX mapping: i) carbon (in blue), j) oxygen (in orange), k) sulfur (in pink), l) phosphorus (in green), m) fluorine (in yellow), n) nickel (in turquoise), o) cobalt (in purple), and p) manganese (in lagoon blue).

The F 1s core-level spectra recorded for the NCM_{811} and $ONCM_{811}$ electrodes, taken at different sputtering depths, are presented in Figure 2b,c, respectively. Generally, both show two distinct peaks: one with a higher intensity at 688.2 eV, which is assigned to -CF_2- and originates from poly(vinylidene difluoride) (PVdF) that has been used as binder (while in the case of $ONCM_{811}$ presumably also including some contribution from the PP10-Li coating),[21] and one with a lower

© 2021 The Authors. Advanced Functional Materials published by Wiley-VCH GmbH

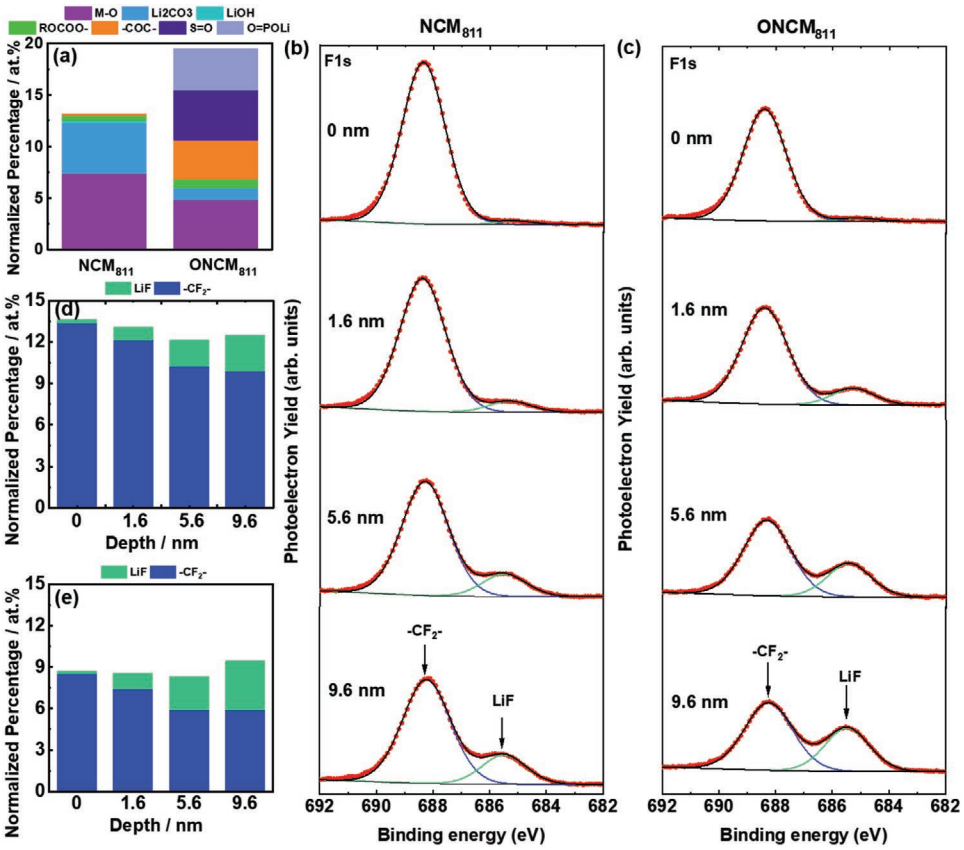

Figure 2. XPS analysis of pristine NCM_{811} and $ONCM_{811}$ electrodes: a) Comparison of the concentration of the different oxygen-containing surface species calculated from O 1s spectra fitting (Figure S3, Supporting Information); F 1s spectra (full scale is 9000) of b) NCM_{811} and c) $ONCM_{811}$ electrodes before sputtering (top) and after increasing sputtering times with an indication of the estimated sputtering depth (from top to bottom); normalized quantitative analysis of the LiF and $–CF_2–$ content for d) NCM_{811} and e) $ONCM_{811}$ pristine electrodes as a function of the sputtering depth.

intensity at 658.5 eV, which is ascribed to the presence of LiF.[22] The appearance of LiF in the pristine electrodes has been reported to be a consequence of the minor dehydrofluorination reaction of PVdF, catalyzed by the alkaline species (such as LiOH and Li_2CO_3) present in the slurry during the electrode coating process, resulting in the formation of HF that reacts at the NCM surface and eventually forms LiF.[21a,23] Prior to the sputtering, the relative contribution is similar for NCM_{811} and $ONCM_{811}$ (i.e., 0.26 and 0.22 at%, respectively – see also Figure 2d,e). However, the relative contribution increases during the Ar^+ sputtering treatment, implying that the LiF formation occurs largely at the NCM surface, which is in line with the earlier reported mechanism. Notably, the relative contribution of LiF after sputtering for 12 min (equivalent to an estimated sputtering depth of 9.6 nm) is higher for $ONCM_{811}$ (3.53 at% vs 2.60 at% for NCM_{811}). In combination with the lower concentration of LiOH and Li_2CO_3 that are (largely) responsible for the formation of LiF,[21a,23] this finding indicates that PP10-Li is strongly bound to the NCM_{811} surface and presumably partially reacting. Such enrichment in LiF (in addition to the PP10-Li coating layer) is expected to have a beneficial effect on the Li^+ transport kinetics, the suppression of transition metal dissolution, and the stability of the interface with the electrolyte.[24]

2.2. Reactivity with Moist Air

Facile storage and handling of cathode active materials (and materials in general) are critical for the battery industry. Thus, we comparatively studied also the evolution of NCM_{811} and $ONCM_{811}$ upon storage under a controlled ambient atmosphere. For this purpose, we exposed the two materials to a controlled relative humidity of 65% for six days. The comparison of the resulting gain in mass reveals that NCM_{811} is more sensitive to such storage conditions, as it is significantly greater compared to $ONCM_{811}$, i.e., 0.55% versus 0.32% (**Figure 3**a), further supporting the beneficial impact of the PP10-Li coating as a physical barrier toward the environment. Subsequently, the gain in mass was investigated in more detail, revealing that the reversible water absorption was 0.15% and 0.16% for NCM_{811} and $ONCM_{811}$ respectively, as determined by thermogravimetric vapor sorption analysis (Figure 3b). The slightly higher reversible water absorption of $ONCM_{811}$ might be explained by the hygroscopic nature of the PP10-Li coating, absorbing more water than the NCM_{811} particles – notably without reacting with the ambient moisture, as it is subsequently released again. In fact, the relatively higher reversible water absorption in combination with the relatively lower gain in mass and the lower contribution of common reaction products such as LiOH and

© 2021 The Authors. Advanced Functional Materials published by Wiley-VCH GmbH

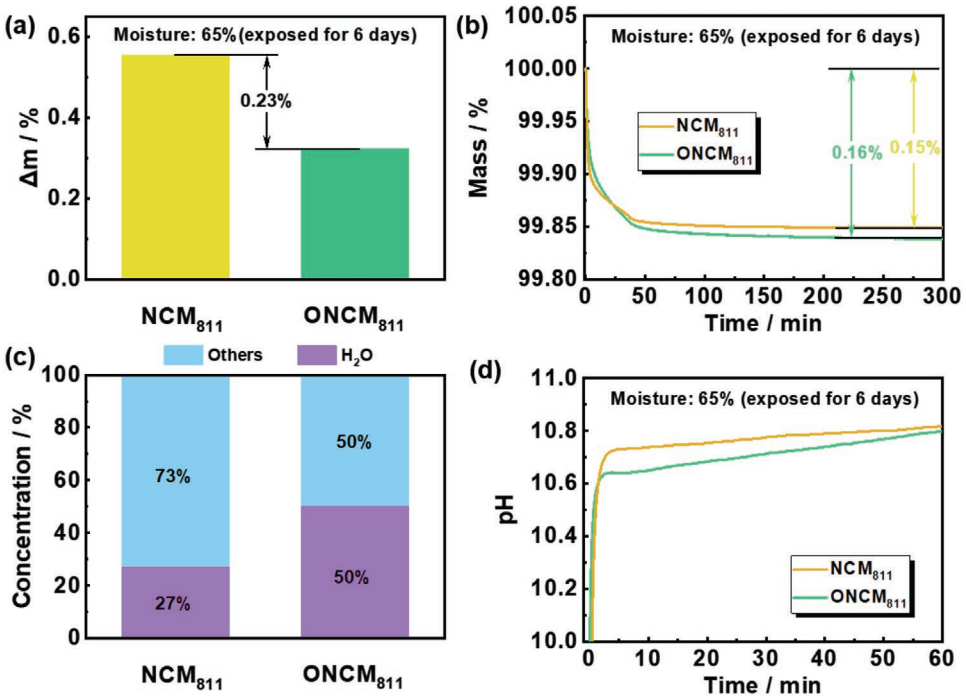

Figure 3. Comparative investigation of the impact of moist air (relative humidity = 65%) upon storage of NCM_{811} and $ONCM_{811}$ powders for six days: a) increase in mass; b) determination of the water content via thermogravimetric vapor sorption analysis; c) analysis of the composition of the species that are responsible for the increase in mass; d) evolution of the pH value as a function of time.

Li_2CO_3 (50% of the overall gained mass, Figure 3c) indicates that the PP10-Li coating suppresses the reactivity with H_2O and CO_2. This is also reflected in the relatively lower increase of the pH value when dispersing the two materials in deionized water (Figure 3d). For NCM_{811}, the pH value jumps to 10.73 after about 3 min and subsequently increases slowly to 10.82 after 60 min, which is lower than for $ONCM_{811}$ with 10.64 and 10.81, respectively. This is in agreement with the lower LiOH and Li_2CO_3 content and the mitigated surface reactivity in the case of $ONCM_{811}$, illustrating a facilitated handling and storage of the PP10-Li-coated material.

2.3. Electrochemical Characterization

As any surface coating naturally impacts the de-/lithiation kinetics, we performed a comparative analysis of NCM_{811} and $ONCM_{811}$ electrodes via cyclic voltammetry (Figure S4, Supporting Information). While both cells generally show high reversibility and the characteristic redox couples, related to the three common phase transitions occurring upon de-/lithiation (see the corresponding discussion in the Supporting Information), the determination of the apparent lithium-ion diffusion coefficient reveals slightly higher values for $ONCM_{811}$ (i.e., 9.7×10^{-8} and 3.9×10^{-8} cm^2 s^{-1} for the delithiation and lithiation, respectively, compared to 8.3×10^{-8} and 3.4×10^{-8} cm^2 s^{-1} for NCM_{811}), highlighting the positive impact of the PP10-Li coating layer on the de-/lithiation kinetics.

In order to investigate how these findings are reflected in the dis-/charge behavior under galvanostatic conditions, half-cells comprising NCM_{811} and $ONCM_{811}$-based positive electrodes were subjected to varying C rates (**Figure 4**). Figure 4a,b provides a comparison of representative dis-/charge profiles at varying C rates from 0.1C to 10C. Generally, the reversible specific capacities are slightly lower for $ONCM_{811}$ compared to NCM_{811} (i.e., 201 vs 203 mAh g^{-1} (0.1C); 195 vs 197 mAh g^{-1} (0.2C); 186 vs 188 mAh g^{-1} (0.5C); 178 vs 180 mAh g^{-1} (1C); 170 vs 172 mAh g^{-1} (2C); 154 vs 156 mAh g^{-1} (5C); 147 vs 148 mAh g^{-1} (7C); and 137 vs 137 mAh g^{-1} (10C)), while the difference is diminishing for higher dis-/charge rates. In fact, the slightly lower capacity at low and medium C rates is assigned to the mass contribution of the PP10-Li coating, which has been included in the calculation of the specific capacity. Accordingly, when normalizing the specific capacity values with regard to the reversible capacity obtained at 0.1C, the values are essentially the same for the low and medium C rates and higher for $ONCM_{811}$ at 10C (Figure 4c), revealing a better rate capability owing to the PP10-Li coating. As a matter of fact, the initial overpotential for the delithiation at elevated dis-/charge rates (2C and higher) is significantly higher for NCM_{811} compared to $ONCM_{811}$ (Figure 4a,b), which underlines the better kinetics in the case of $ONCM_{811}$ and is in agreement with the results of the cyclic voltammetry experiments. To investigate the impact of the PP10-Li coating on the long-term cycling performance, both cells were subsequently subjected to 500 cycles at 1C (Figure 4d). Initially, the capacity for the NCM_{811} cell is slightly higher, as expected from the rate capability test, but it rapidly fades after about 460 cycles, resulting in a capacity retention of only 77.6%. This fading is accompanied by substantial decrease in Coulombic efficiency (CE) down to 99.09%, lowering the average CE to 99.66% upon 500 cycles. Accordingly, the rapid capacity fading toward the end of the

© 2021 The Authors. Advanced Functional Materials published by Wiley-VCH GmbH

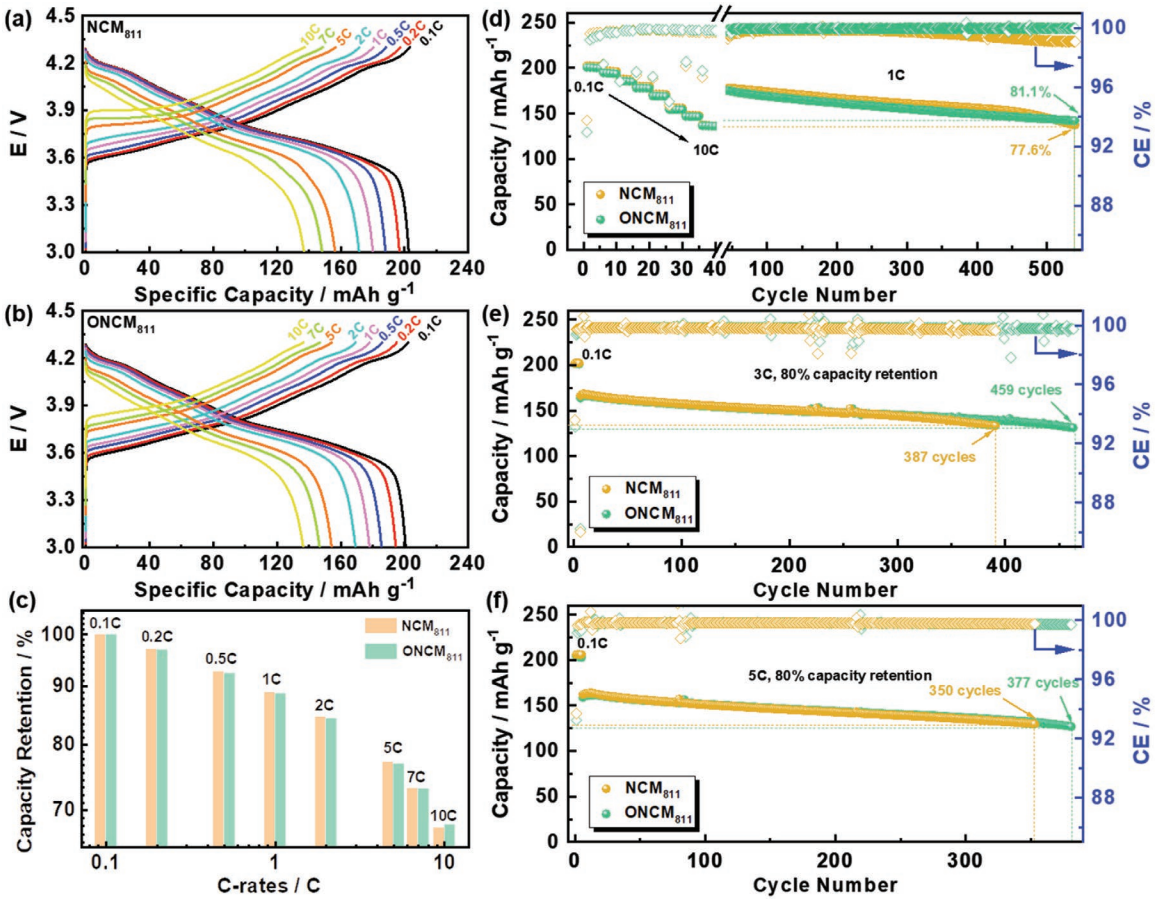

Figure 4. Electrochemical characterization at 20°C: a,b) Representative dis-/charge profiles (2nd cycle at each given C rate) of cells comprising (a) NCM_{811} and (b) $ONCM_{811}$ as the active material for the positive electrode at varying C rates; c) comparison of the normalized capacity retention at different C rates with regard to the capacity obtained at 0.1C; d) evaluation of the rate capability and cycling stability at 1C after applying varying C rates with an indication of the capacity retention after 500 cycles at 1C; (e,f) valuation of the cycling stability at e) 3C and f) 5C after three formation cycles at 0.1C with an indication after how many cycles a capacity retention of 80% is reached.

cycling test is attributed to detrimental side reactions at the electrode|electrolyte interface (including newly formed interfaces due to microcracks evolving in the NCM_{811} particles) and their detrimental impact on the NCM_{811} active material and its crystal structure.[6,25] Differently, the cycling performance of $ONCM_{811}$ is very stable for 500 cycles with a capacity retention of 81.1% and no pronounced fading after 500 cycles at 1C. This superior performance is also reflected in the very high average CE of 99.96%, indicating that the application of the PP10-Li coating layer leads to suppressed side reactions with the electrolyte and preserves a stable electrode|electrolyte interface. Subsequently, we studied also the long-term constant current cycling at elevated C rates of 3C (Figure 4e) and 5C (Figure 4f). Also under these conditions, the $ONCM_{811}$-comprising cells show a substantially enhanced cycling stability (and essentially the same capacity). The cut-off criterion of 80% capacity retention is reached after 459 cycles (3C) and 377 cycles (5C), compared to 387 cycles (3C) and 358 cycles (5C) for the NCM_{811}-based cells.

Subsequently, we studied the cycling performance at elevated temperatures of 40 and 60 °C (**Figure 5**) to stress the beneficial impact of the PP10-Li coating. At 40 °C (Figure 5a), both NCM_{811} and $ONCM_{811}$ provide higher capacities than at 20 °C owing to the increased Li^+ diffusion and transport kinetics. However, during the constant current cycling at 3C, the NCM_{811}-based cell shows an increased capacity fading after about 130 cycles and the 80% capacity retention criterion is reached after only 176 cycles, whereas the $ONCM_{811}$-based cell hits this limit after 221 cycles. The superior cycling stability is even more evident when increasing the ambient temperature to 60 °C (Figure 5b), i.e., a temperature that marks the onset of electrolyte decomposition and triggers substantial side reactions at the electrode|electrolyte interface.[26] While the rate capability is generally very high for both NCM_{811} and $ONCM_{811}$ and better than at 20 °C with, e.g., more than 180 mAh g^{-1} at 10C owing to the greater kinetics, the CE is much higher for $ONCM_{811}$ and the cut-off criterion of 80% capacity retention is reached after 180 cycles at 1C (following to the rate capability test), while the NCM_{811}-based cell fades rapidly and reaches this criterion after only 15 cycles. These results further highlight the highly advantageous effect of the PP10-Li coating on the stabilization of the interface with the electrolyte, successfully suppressing severe side reactions and active material decay.

© 2021 The Authors. Advanced Functional Materials published by Wiley-VCH GmbH

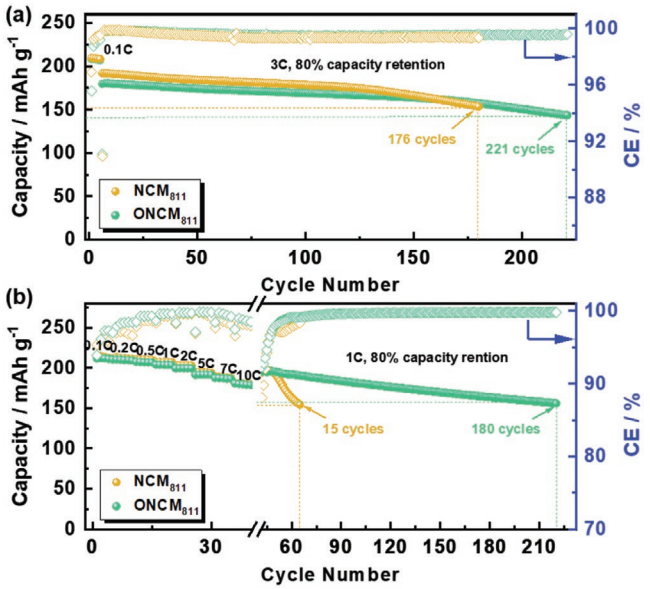

Figure 5. Electrochemical characterization of half-cells comprising NCM_{811} and $ONCM_{811}$ as the active material for the positive electrode a) at 40°C, applying a constant dis-/charge rate of 3C after three formation cycles at 0.1C, with an indication of the cycle number at which a capacity retention of 80% is reached, and b) at 60°C, applying varying dis-/charge rates, followed by constant current cycling at 1C with an indication after how many cycles a capacity retention of 80% is reached.

2.4. Ex Situ Investigation of the (O)NCM_{811} Surface

To unveil how the application of the PP10-Li coating enhances the electrochemical performance, the electrodes cycled according to the testing protocol shown in Figure 4d were eventually analyzed via SEM/EDX. The SEM images of pristine $ONCM_{811}$ and NCM_{811} electrodes are presented in Figure S5 (Supporting Information) and the ex situ SEM data are shown in Figure S6 (Supporting Information). Alike the SEM and TEM data discussed earlier (Figure 1), the surface of the pristine $ONCM_{811}$ particles appears smoother and the edges of the primary nanograins are less apparent (Figure S5a,b, Supporting Information) compared to the SEM images taken for NCM_{811} (Figure S5c,d, Supporting Information) due to the presence of the PP10-Li coating. After cycling (Figure S6, Supporting Information), however, the surface of the NCM_{811} electrodes appears much smoother than prior to cycling, indicating the formation of a rather thick cathode electrolyte interphase (CEI), while the surface morphology of the $ONCM_{811}$ electrodes is largely retained. In fact, the ex situ SEM/EDX analysis of the cycled $ONCM_{811}$ electrodes (Figure S7, Supporting Information), in particular the homogenous elemental distribution of S, for which PP10-Li is the only source (while the other elements are found also for NCM_{811}, Figure S8, Supporting Information), confirms that the coating layer is well preserved, even after such extended cycling for more than 500 cycles.

For a closer look at the particle surface, we performed also ex situ TEM measurements on these cycled electrodes (**Figure 6**). While it is generally difficult to distinguish between the CEI

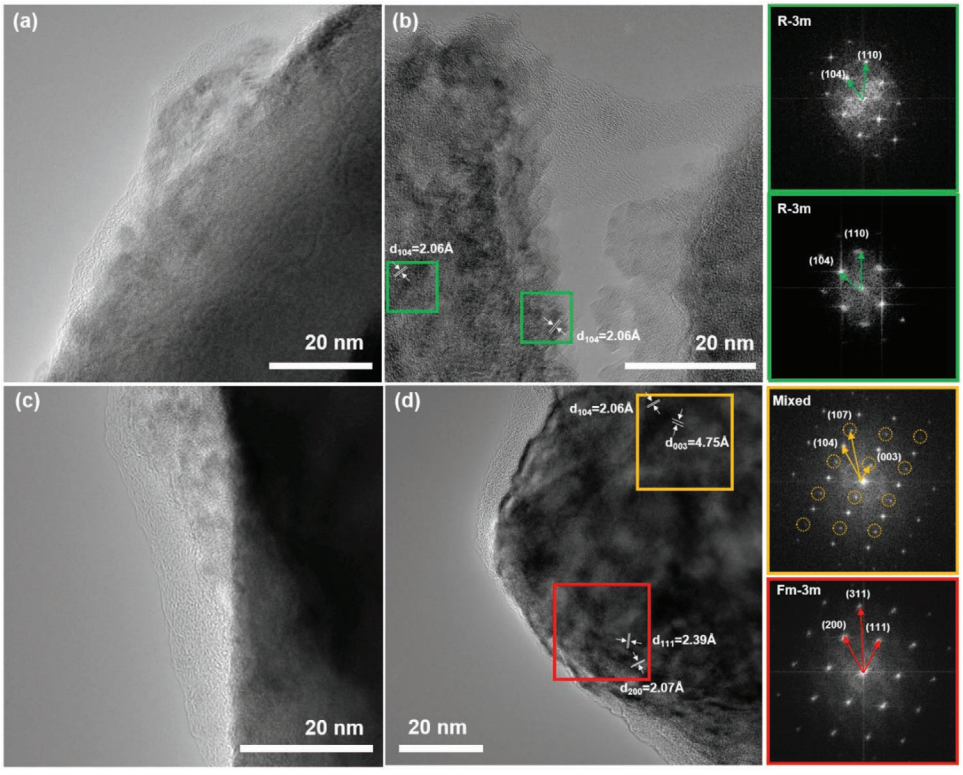

Figure 6. Ex situ TEM analysis of cycled a,b) $ONCM_{811}$ and c,d) NCM_{811} at different magnifications. In (b) and (d) characteristic lattice spacing values are indicated and the corresponding FFT patterns of selected areas highlighted by the colored frames are provided on the right.

© 2021 The Authors. Advanced Functional Materials published by Wiley-VCH GmbH

layer and the PP10-Li coating due to the amorphous nature of both phases, the amorphous surface layer is clearly thinner in the case of $ONCM_{811}$ (Figure 6a) compared to NCM_{811} (Figure 6c) – despite the contribution of the PP10-Li coating in the former case, indicating a pronounced electrolyte decomposition and CEI formation for NCM_{811}. Moreover, when analyzing the crystal structure of the $ONCM_{811}$ particles in the bulk and the near-surface region (Figure 6b), the resulting FFT patterns confirm that the layered (*R*-3*m*) structure is retained.[9c,27] Differently, for the cycled NCM_{811} particles (Figure 6d), the FFT patterns reveal the transition from the layered (*R*-3*m*) structure to the rock-salt (*Fm*-3*m*) structure[28] in the near-surface region (red frame) and a mix of the two crystalline phases in the bulk (orange frame). It is noteworthy that the transition from the layered to the electrochemically inactive rock-salt structure[9c] appears complete for several tens of nanometers from the particle surface toward the particle core, providing an explanation for the pronounced capacity fading in the case of NCM_{811}.

Complementarily, we conducted also an ex situ XPS depth-profiling analysis of the cycled NCM_{811} and $ONCM_{811}$ electrodes to gain additional insights into the thickness and composition of the CEI layer (**Figure 7**). The O 1s and F 1s spectra for NCM_{811} are depicted in Figure 7a,b and the O 1s and F 1s spectra for $ONCM_{811}$ are presented in Figure 7c,d (including in both cases the XPS data for the pristine electrodes at the top for comparison). Generally, for both NCM_{811} and $ONCM_{811}$,

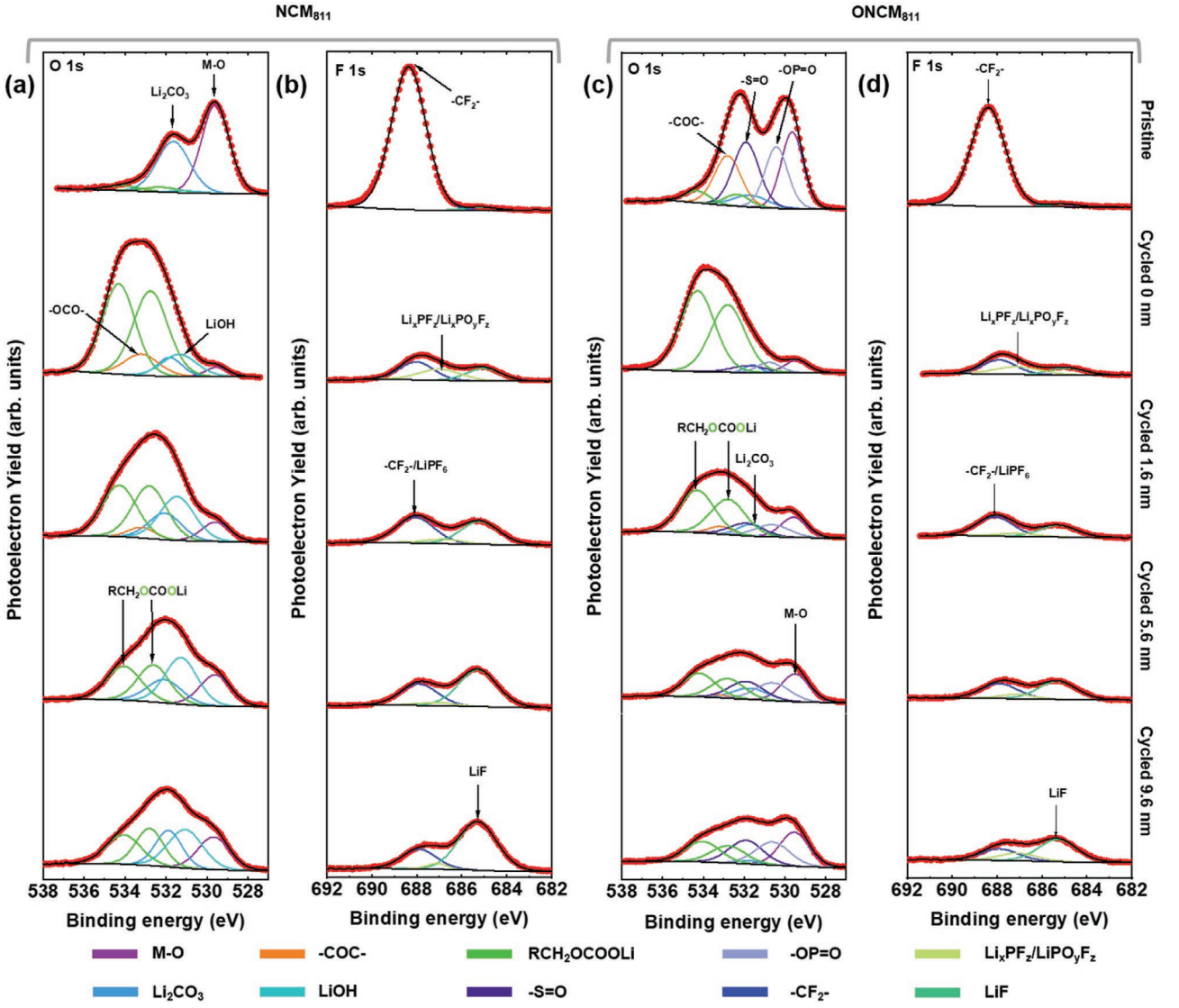

Figure 7. Ex situ XPS analysis: a) O 1s and b) F 1s spectra of NCM_{811} cycled electrodes; c) O 1s and d) F 1s spectra of $ONCM_{811}$ cycled electrodes. In all cases, the spectra shown at the top have been obtained for pristine electrodes and serve as reference. The spectra obtained for cycled electrodes prior to any sputtering are shown in the row below and in the subsequent rows the sputtering time has been stepwise increased (from top to bottom, with an indication of the estimated sputtering depth). The color coding for the fitted contributions is shown below the XPS spectra. It should be noted that the scale for photoelectron yield at the y axis has been kept constant for all O 1s (6400) and F 1s spectra (9000). The O 1s spectra of the pristine NCM_{811} and $ONCM_{811}$ electrodes are the same as those presented in Figure S3 (Supporting Information), but shown here once again for the sake of convenience when comparing the XPS spectra before and after cycling.

© 2021 The Authors. Advanced Functional Materials published by Wiley-VCH GmbH

the spectra recorded prior to any sputtering reveal contributions from organic (e.g., $RCH_2OCOOLi$ and -COC-) and inorganic (e.g., LiOH, Li_2CO_3, LiF, and $Li_xPF_z/Li_xPO_yF_z$) electrolyte decomposition products. In line with the XPS data obtained for the pristine electrodes, however, the $ONCM_{811}$ electrodes show substantially less Li_2CO_3 and essentially no LiOH. Furthermore, the $ONCM_{811}$ electrodes show generally less decomposition products and a greater intensity for the M-O contribution, indicating that the CEI is thinner overall. Besides, contributions from -S = O and -OP = O are observed for cycled $ONCM_{811}$ electrodes, further corroborating that the PP10-Li layer is preserved on the particle surface. Upon sputtering the M-O contribution increases in both cases, confirming that the CEI layer is increasingly removed. Simultaneously, the relative contribution of the organic electrolyte decomposition products is gradually decreasing, though more pronounced for $ONCM_{811}$, while the contribution of LiF is increasing in both cases, which is more pronounced for NCM_{811}, however. This observation in combination with the initially higher LiF concentration for the pristine $ONCM_{811}$ electrodes further supports the conclusion that there is more electrolyte decomposition in the case of NCM_{811}. Additionally, the contribution of Li_2CO_3 is increasing particularly for NCM_{811}, and the contribution of the PP10-Li-related peaks (i.e., -S = O and -OP = O) is increasing for $ONCM_{811}$. These findings globally indicate that the outer CEI layer is more organic in nature, while the inner layer is rather composed of inorganic products, which is in line with earlier CEI studies.[29] Moreover, they show that the surface chemistry of the pristine electrodes is somehow retained, which includes the preservation of the PP10-Li coating layer at the intimate particle surface.

2.5. Evaluation of the Thermal Stability

Finally, we studied also the impact of the PP10-Li coating on the thermal behavior of the delithiated NCM_{811} and $ONCM_{811}$ electrodes (charged to 4.3 V) in presence of the electrolyte by differential scanning calorimetry (DSC, **Figure 8**). Generally, the onset temperature for the heat evolution is significantly lower in both cases compared to the base electrolyte only (in grey), revealing the characteristic decomposition profile for DEC,[30] which underlines the greater reactivity of the latter in contact with delithiated NCM.[31] Besides, it is fairly similar for both active materials, while the overall heat evolution is substantially lower for $ONCM_{811}$ (1139.0 J g^{-1}) compared to NCM_{811} (1321.7 J g^{-1}). In fact, the DSC curve recorded for PP10-Li only (in red) does not show any exothermic features up to 300 °C, only a glass transition and an endothermic peak at ≈230 and ≈274 °C, respectively, further highlighting the beneficial impact of the coating – not only for the electrochemical performance, but moreover regarding safety.

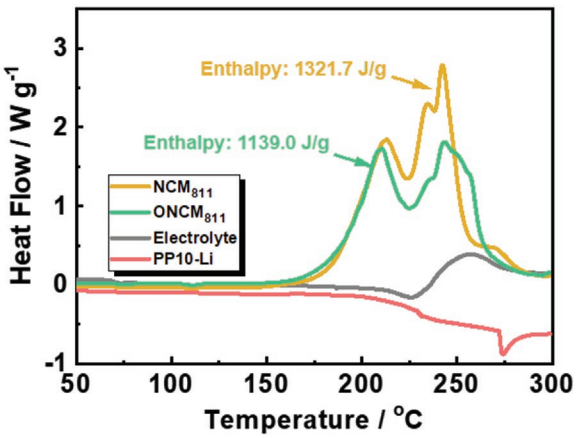

Figure 8. DSC profiles of (partially) delithiated NCM_{811} (in yellow) and $ONCM_{811}$ (in green) electrodes in presence of the electrolyte. The delithiation cut-off was set to 4.3 V. For comparison, also the DSC profiles obtained for the pure electrolyte (in gray) and pure PP10-Li (in red) are shown.

3. Conclusions

The PP10-Li coating addresses the most challenging issues of Ni-rich NCM, i.e., the poor cycling stability and the low thermal stability, by suppressing the undesired surface reactions with moist air (i.e., H_2O and CO_2) upon storage and processing as well as with the electrolyte upon cycling, especially at elevated temperatures. As a result, PP10-Li-coated NCM_{811} ($ONCM_{811}$) provides a substantially enhanced electrochemical performance in terms of rate capability, capacity retention, and Coulombic efficiency (99.96% vs 99.66%) owing to the favorable de-/lithiation kinetics as well as the stabilized electrode|electrolyte interface and interphase. Most remarkable is certainly the improvement in capacity retention at 60 °C from 15 cycles (NCM_{811}) to 180 cycles ($ONCM_{811}$). In combination with the substantially reduced heat evolution, this finding particularly highlights the beneficial impact of the coating also concerning safety. We may anticipate that the use of well-designed lithiated polymer coatings, as reported herein for the first time, is an effective strategy for today's and tomorrow's cathode materials.

4. Experimental Section

Chemicals for the Synthesis of PP10-Li: 4,4'-difluorodiphenyl sulfone (DFDPS, >98%) and 4,4'-biphenol (BP, 99%) were purchased from Alfa Aesar and recrystallized from isopropanol before use. Toluene, potassium carbonate (K_2CO_3, 99%), calcium hydride (CaH_2, 98%), methanol, hydrochloric acid (HCl, 36.5 wt%), and lithium hydroxide monohydrate ($LiOH{\cdot}H_2O$, 98%) were purchased from Alfa Aesar and used as received. Dichloromethane (DCM) was purchased from Sigma Aldrich and freshly distilled from CaH_2 before use. Hexafluorobenzene (HFB, 99%), anhydrous dimethylacetamide (DMAc), *N*-methyl-2-pyrrolidone (NMP, >99%), bromine (Br_2, 99.99%), anhydrous acetic acid (CH_3COOH, 99.8%), palladium acetate ($Pd(OAc)_2$, >99.9), triphenylphosphine (TPP, 99%), diethyl phosphite (DEP, 98%), and dicyclohexylmethylamine (DCHMA, 97%) were purchased from Sigma Aldrich and used as received unless otherwise noted.

Synthesis of PP10-Li: The complete synthesis of PP10-Li is shown in Figure S9 (Supporting Information) and described in the following in more detail.

Synthesis of HFB End-Capped PES10: HFB end-capped PES10 was synthesized by modifying a one-pot two-reaction procedure reported elsewhere.[32] In a typical protocol (Figure S9, Supporting Information)), a 100-mL three-neck round-bottom flask, equipped with a mechanical stirrer, a condenser, an argon inlet/outlet, and a Dean-Stark trap, was charged with DFDPS (4.000 g, 15.732 mmol) and BP (3.052 g, 16.388 mmol). DMAc (28 mL) was added to obtain a solid concentration of 25% (wt/v). When all solid components were completely dissolved, K_2CO_3 (6.79 g, 0.0492 mol)

© 2021 The Authors. Advanced Functional Materials published by Wiley-VCH GmbH

and 14 mL of toluene, serving as azeotroping agent, were added. The DMAc to toluene ratio was 2:1 v/v. The reaction bath was heated to 150 °C and kept at this temperature for 4 h to dehydrate the system. Subsequently, the bath temperature was slowly raised to 160 °C to remove the toluene. Afterward, the temperature of the reaction bath was decreased to 120 °C and the polymerization was allowed to proceed for 24 h. In a next step, the reaction temperature was set to 70 °C and 2.44 g (13.11 mmol) of HFB were added, while the argon purge was stopped at this point owing to the low boiling point of HFB. The reaction was allowed to proceed for 12 h. Then, the reaction mixture was precipitated into 2 L of 1 M HCl aqueous solution with magnetic agitation for 8 h, filtered, and rinsed with distilled water until reaching a neutral pH value. The resulting white powder was dried under vacuum at 80 °C for 24 h to obtain the final product (M_n = 10 600 g mol^{-1}, M_w = 21 500 g mol^{-1}, polydispersity index (M_w/M_n) = 2.0). ^{1}H and ^{19}F nuclear magnetic resonance (NMR) spectra of HFB end-capped PES10 are shown in Figure S10 (Supporting Information).

^{1}H-NMR ($CDCl_3$): δ (ppm) 7.92 (d), 7.61 (d), 7.54 (d), 7.14 (d), 7.10 (d), 7.06 (d).

^{19}F-NMR ($CDCl_3$): δ (ppm) –153.78 (d), –159.5 (m), –161.75 (m).

Synthesis of Brominated PES10 (BPES10): The bromination of PES10 (yielding BPES10) was conducted at room temperature using elemental bromine as the brominating agent in the presence of acetic acid (Figure S9, Supporting Information)). In a typical protocol, 5.000 g of PES10 (12.10 mmol of the biphenyl unit) was loaded into a 250 mL three-neck round-bottom flask, equipped with a mechanical stirrer, a condenser, an argon inlet, and a funnel. First, 90 mL of DCM, distilled from CaH_2, and 9 mL of acetic acid (10% v/v to DCM) were added. After the polymer was completely dissolved, 9.36 mL of bromine (Br_2; 0.182 mol) was added dropwise to the reaction mixture, followed by strong stirring, and the reaction was allowed to proceed at room temperature for 16 h. Subsequently, the reaction mixture was precipitated into 1000 mL of methanol, washed three times with methanol to remove excessive bromine, and kept under continuous agitation for 16 h. Afterward, the polymer was filtered and rinsed again with methanol until any residual bromine was completely removed. The final product, i.e., BPES10, was dried under vacuum at 80 °C for 24 h. ^{1}H and ^{19}F NMR spectra of BPES10 are shown in Figure S11 (Supporting Information).

^{1}H-NMR (DMSO.d6): δ (ppm) 8.14 (s), 8.03 (d), 7.95 (d), 7.79 (d), 7.49 (d), 7.34 (d), 7.10 (d).

^{19}F-NMR (DMSO.d6): δ (ppm) –137.76 (s), –138.14 (m), –153.23 (s), –153.67 (m), –160.69 (t).

Synthesis of Lithium Phosphonate Functionalized PES10 (PP10-Li): The phosphonate functions were tethered to the brominated BPES10 using a palladium-catalyzed coupling reaction (Figure S9, Supporting Information)). In a typical procedure, BPES10 (2.00 g, 7.19 mmol Br), $Pd(OAc)_2$ (80.7 mg, 0.36 mmol), TPP (0.283 g, 1.08 mmol), and anhydrous DMAc (40 mL) were loaded into a 100-mL two-neck round-bottom flask equipped with an argon inlet/outlet and a magnetic bar. The reaction mixture was heated to 95 °C under strong stirring to obtain a homogeneous solution. Subsequently, DEP (4.6 mL, 36.0 mmol) and DCHMA (4.6 mL, 21.6 mmol) were added, and the reaction was allowed to proceed at this temperature for 48 h. The reaction mixture was precipitated into ethanol, washed several times with ethanol, and filtered to obtain a white solid, which was dried under vacuum at 80 °C for 24 h, eventually yielding the ethyl phosphonate form of PES10 (i.e., PP10-Et, 95% yield). PP10-Et (1.00 g, 2.98 mmol of the -$PO(OC_2H_5)_2$ function) was boiled in a 36.5% HCl aqueous solution for 4 h and washed several times with distilled water to remove any residual HCl. The resulting product, i.e., PES10 functionalized with phosphonic acid (i.e., PP10-H) was dispersed in a 0.5 M aqueous solution of LiOH, washed several times with distilled water, filtered, and dried under vacuum at 80 °C for 24 h to finally obtain the targeted PP10-Li (93% yield). ^{1}H and ^{19}F NMR spectra of PP10-Et as intermediate species are shown in Figure S12 (Supporting Information) and the ^{1}H NMR spectrum of the acidic form PES10 is presented in Figure S13 (Supporting Information). The comparison of the two spectra reveals the absence of peak 6 and 7, observed in Figure S12 (Supporting Information) and assigned to the ethyl groups, in Figure S13 (Supporting Information), indicating the complete conversion to the acidic form. The ion-exchange capacity (IEC) of PP10-Li as the final product was determined via ^{1}H NMR spectroscopy and the results are provided in Table S1 (Supporting Information).

^{1}H-NMR (DMSO.d6): δ (ppm) 8.03 (m), 7.95 (d), 7.74 (m), 7.31 (m), 7.21 (m), 7.13 (d), 3,98 (q), 1,05 (t).

^{19}F-NMR (DMSO.d6): δ (ppm) –155.17 (d), –160.70 (m), –162.39 (m).

Preparation of PP10-Li-Coated NCM_{811} ($ONCM_{811}$): First, 0.1 g of PP10-Li were introduced into a 50-mL round-bottom flask. 10.0 mL of NMP were added and the mixture was heated to 120 °C. Subsequently, 4.0 mL of deionized water (DIW) were added dropwise until PP10-Li was completely dissolved. Afterward, the water was removed via azeotropic distillation. For the drying step, 10 mL of toluene were added and the solution was placed in a Dean Stark system. The mixture was heated up to 160 °C and kept at this temperature under reflux overnight. Finally, any residual water and the toluene were removed to yield PP10-Li dissolved in NMP only.

1 g of NCM_{811} (a pre-commercial material that was generally stored under argon in a glass vial and the glass vial was stored in a dry room with the dew point being always below –60 °C at 20 °C ambient temperature) was added into 2 mL of the PP10-Li in NMP solution (corresponding to 2 wt% of PP10-Li with regard to the mass of NCM_{811}). The resulting dispersion was stirred slowly and heated up to 80 °C in order to slowly evaporate the NMP, finally yielding the PP10-Li-coated NCM_{811}, herein referred to as $ONCM_{811}$.

Physicochemical Characterization: ^{1}H and ^{19}F NMR spectroscopy was performed using a Bruker Ascend 400 apparatus. Size-exclusion chromatography (SEC) with a multi angle light scattering detector (MALS) was conducted at room temperature on a Waters 590 GPC equipped with a Waters 410 differential refractometer and a Waters 745 Data Module. A 1 M solution of $NaNO_3$ in dimethylformamide (DMF) was used as solvent, applying a flow rate of 1 mL min^{-1}. The 1 wt% solution of PES10 was filtered using a 0.45 mm Millipore polytetrafluoroethylene filter and three Ultrastyragel columns of 5×10^2, 10^3, and 10^4 Å. The calibration was performed using polystyrene standards.

The crystal structure of NCM_{811} and $ONCM_{811}$ was studied via X-ray diffraction (XRD) – on both powders and electrodes – using a Bruker D8 Advance with Cu-Kα radiation of λ = 0.15 406 nm. The morphology of NCM_{811} and $ONCM_{811}$ was investigated by scanning electron microscopy (SEM; ZEISS EVO MA 10), equipped with an energy-dispersive X-ray (EDX) spectrometer (Oxford Instruments X-MaxN, 50 mm^2, 15 kV), and high-resolution transmission electron microscopy (HRTEM at 300 kV; FEI Titan 80–300 with image *Cs*-corrector). X-ray photoelectron spectroscopy (XPS) was conducted using a Phoibos 150 XPS spectrometer (SPECS) equipped with a micro-channel plate and Delay Line Detector (DLD) and a monochromatic Al-Kα ($h\nu$ = 1,487 eV) X-ray source. The scans were acquired in a Fixed Analyzer Transmission mode with an X-ray source power of 200 W (15 kV), 30 eV pass energy and 0.1 eV energy steps. The depth profiling was performed using a focused 5 keV Ar^+ ion gun and sputtering rate of 0.8 nm min^{-1}. Fitting of the spectra was carried out with the CasaXPS software, using a nonlinear Shirley-type background and 70% Gaussian and 30% Lorentzian profile functions. The spectra were calibrated by means of the C 1s peak of the adventitious carbon, centered at 284.8 eV, and the intensity was normalized. The determination of the water content was carried out via thermogravimetric vapor sorption analysis (Q5000SA, TA Instruments). The samples were kept at 25 °C for 10 min for equilibration, before being heated to 60 °C with a heating rate of 1 °C min^{-1}. Then, the samples were kept at a constant temperature for 300 min to evaporate all the water.

Electrode Preparation and Cell Assembly: The $ONCM_{811}$ and NCM_{811} electrodes were prepared by dispersing the active material (92 wt%), C-NERGY Super C65 (TIMCAL, 4 wt%), and polyvinylidene fluoride (PVdF 6020, Solvay, 4 wt%) in NMP (Aldrich) with a solid:liquid ratio of 1:1 (wt/wt). The intimately mixed slurries were cast on Al foil (battery grade) using a laboratory-scale doctor-blade. The wet electrodes were initially pre-dried at 60 °C to remove the NMP. Subsequently, disc-shaped electrodes were punched and subjected to a further drying under vacuum at 100 °C for 12 h (Büchi). The average active material mass

© 2021 The Authors. Advanced Functional Materials published by Wiley-VCH GmbH

loading was 2.2 ±0.2 mg cm^{-2}. All electrode preparation steps were performed in a dry room with the dew point always being below –60 °C at an ambient temperature of 20 °C.

The electrochemical characterization was conducted in CR2032 coin cells (Hohsen). Metallic lithium (Honjo, battery grade, 500 µm thickness) was used as the counter electrode, 1 M $LiPF_6$ dissolved in a 1:1 (by weight) mixture of ethylene carbonate (EC) and diethyl carbonate (DEC) (1:1 wt/wt) with 1 wt% of vinylene carbonate (VC), supplied by BASF, was used as the electrolyte, and a single-layer polyethylene membrane (ASAHI KASEI, Hipore SV718) was used as separator. All coin cells were assembled in an argon-filled glove box (with O_2 <0.1 ppm and H_2O < 0.1 ppm).

Electrochemical Characterization: All galvanostatic tests were conducted in a voltage range from 3.0 to 4.3 V using a Maccor battery tester (Maccor 4000). The ambient temperature (i.e., 20, 40, and 60 °C) was controlled by a climatic chamber (Binder). A dis-/charge rate of 1C corresponds to a specific current of 200 mA g^{-1}. Cyclic voltammetry (CV) was performed using a multi-channel potentiostat (VMP Biologic). The voltage range was set to 3.0–4.3 V and the temperature was 20 °C. For the initial five cyclic sweeps, a lower scan rate of 0.1 mV s^{-1} was applied, followed by varying scan rates from 0.1 to 1.5 mV s^{-1}.

Ex Situ Characterization: For the ex situ SEM, XPS, and TEM analysis, the cycled cells (540 cycles at varying C rates and 20 °C – see Figure 4d) were opened in an argon-filled glove box (with O_2 <0.1 ppm and H_2O <0.1 ppm). The electrodes were washed several times with dimethyl carbonate (DMC) to remove any residual electrolyte and then dried in a glove box. For the sample transfer to the corresponding instrument, specific sample holders were used which prohibit the contact with the ambient atmosphere. For the ex situ SEM, XPS, and TEM analysis, the same experimental parameters were used as for the pristine samples. The thermal stability of NCM_{811} and $ONCM_{811}$ was determined by differential scanning calorimetry (DSC; Discovery TA instruments). The electrodes were initially cycled galvanostatically in half-cells at 0.1C for three cycles, and then charged to 4.3 V with a subsequent constant voltage step with a cut-off current equivalent to 0.01C. The cells were disassembled in a glove box and rinsed with DMC to remove any residual electrolyte. About 7–8 mg of the electrode coating were scratched from the electrodes and hermetically sealed in 30-µL high-pressure gold-plated copper stainless steel vessels, together with some fresh electrolyte. Prior to the heating the samples up to 300 °C at a heating rate of 3 °C min^{-1}, an equilibration step of 10 min at 40 °C was applied.

Supporting Information

Supporting Information is available from the Wiley Online Library or from the author.

Acknowledgements

The authors would like to acknowledge the financial support from the Federal Ministry of Education and Research (BMBF) within the FestBatt project (03XP0175B), the Helmholtz Association for the basic funding, the French National Research Agency within the NSPEM project (ANR-16-CE05-0016), and the Centre of Excellence of Multifunctional Architectured Materials "CEMAM" AN-10-LABX-44–01). This research was supported by the Industry University Convergence Area R&D Program from the Ministry of Trade, Industry and Energy through Chungbuk Energy Institute for Industry-University Convergence (2021R1A4A20016871 and CBE-2020-05).

Open access funding enabled and organized by Projekt DEAL.

Conflict of Interest

The authors declare no conflict of interest.

Data Availability Statement

The data that support the findings of this study are available from the corresponding author upon reasonable request.

Keywords

cathodes, coating, lithium batteries, Ni-rich NCM, polymers

Received: June 3, 2021
Revised: June 28, 2021
Published online:

[1] a) J. Kim, H. Lee, H. Cha, M. Yoon, M. Park, J. Cho, *Adv. Energy Mater.* **2018**, *8*, 1702028; b) A. Manthiram, B. Song, W. Li, *Energy Storage Mater.* **2017**, *6*, 125.

[2] a) F. Schipper, E. M. Erickson, C. Erk, J.-Y. Shin, F. F. Chesneau, D. Aurbach, *J. Electrochem. Soc.* **2016**, *164*, A6220; b) A. Manthiram, J. C. Knight, S.-T. Myung, S.-M. Oh, Y.-K. Sun, *Adv. Energy Mater.* **2016**, *6*, 1501010; c) S. Kalluri, M. Yoon, M. Jo, H. K. Liu, S. X. Dou, J. Cho, Z. Guo, *Adv. Mater.* **2017**, *29*, 1605807; d) S. Neudeck, F. Walther, T. Bergfeldt, C. Suchomski, M. Rohnke, P. Hartmann, J. Janek, T. Brezesinski, *ACS Appl. Mater. Interfaces* **2018**, *10*, 20487; e) M. Armand, P. Axmann, D. Bresser, M. Copley, K. Edström, C. Ekberg, D. Guyomard, B. Lestriez, P. Novák, M. Petranikova, *J. Power Sources* **2020**, *479*, 228708.

[3] Z. Chen, G.-T. Kim, D. Bresser, T. Diemant, J. Asenbauer, S. Jeong, M. Copley, R. J. Behm, J. Lin, Z. Shen, S. Passerini, *Adv. Energy Mater.* **2018**, *8*, 1801573.

[4] Z. Chen, D. Chao, J. Lin, Z. Shen, *Mater. Res. Bull.* **2017**, *96*, 491.

[5] a) C. S. Yoon, H.-H. Ryu, G.-T. Park, J.-H. Kim, K.-H. Kim, Y.-K. Sun, *J. Mater. Chem. A* **2018**, *6*, 4126; b) B.-B. Lim, S.-T. Myung, C. S. Yoon, Y.-K. Sun, *ACS Energy Lett.* **2016**, *1*, 283; c) C. S. Yoon, K.-J. Park, U.-H. Kim, K. H. Kang, H.-H. Ryu, Y.-K. Sun, *Chem. Mater.* **2017**, *29*, 10436; d) K. Min, K. Park, S. Y. Park, S. W. Seo, B. Choi, E. Cho, *Sci. Rep.* **2017**, *7*, 7151.

[6] H.-H. Ryu, K.-J. Park, C. S. Yoon, Y.-K. Sun, *Chem. Mater.* **2018**, *30*, 1155.

[7] J. Sicklinger, M. Metzger, H. Beyer, D. Pritzl, H. A. Gasteiger, *J. Electrochem. Soc.* **2019**, *166*, A2322.

[8] Z. Chen, G.-T. Kim, D. Chao, N. Loeffler, M. Copley, J. Lin, Z. Shen, S. Passerini, *J. Power Sources* **2017**, *372*, 180.

[9] a) H. Yang, K. Wu, G. Hu, Z. Peng, Y. Cao, K. Du, *ACS Appl. Mater. Interfaces* **2019**, *11*, 8556; b) A. T. Freiberg, J. Sicklinger, S. Solchenbach, H. A. Gasteiger, *Electrochim. Acta* **2020**, *346*, 136271; c) Z. Chen, G.-T. Kim, Z. Wang, D. Bresser, B. Qin, D. Geiger, U. Kaiser, X. Wang, Z. X. Shen, S. Passerini, *Nano Energy* **2019**, *64*, 103986.

[10] a) Y.-K. Sun, S.-T. Myung, M.-H. Kim, J. Prakash, K. Amine, *J. Amer. Chem. Soc.* **2005**, *127*, 13411; b) S.-T. Myung, K.-S. Lee, D.-W. Kim, B. Scrosati, Y.-K. Sun, *Energy Environ. Sci.* **2011**, *4*, 935.

[11] a) X. Xu, L. Xiang, L. Wang, J. Jian, C. Du, X. He, H. Huo, X. Cheng, G. Yin, *J. Mater. Chem. A* **2019**, *7*, 7728; b) U.-H. Kim, H.-H. Ryu, J.-H. Kim, R. Mücke, P. Kaghazchi, C. S. Yoon, Y.-K. Sun, *Adv. Energy Mater.* **2019**, *9*, 1970046.

[12] a) P. Kang-Joon, J. Hun-Gi, K. Liang-Yin, K. Payam, Y. C. S. , S. Yang-Kook, *Adv. Energy Mater.* **2018**, *8*, 1801202; b) K. Min, S.-W. Seo, Y. Y. Song, H. S. Lee, E. Cho, *Phys. Chem. Chem. Phys.* **2017**, *19*, 1762; c) T. Weigel, F. Schipper, E. M. Erickson, F. A. Susai, B. Markovsky, D. Aurbach, *ACS Energy Lett.* **2019**, *4*, 508.

[13] a) D. Becker, M. Börner, R. Nölle, M. Diehl, S. Klein, U. Rodehorst, R. Schmuch, M. Winter, T. Placke, *ACS Appl. Mater. Interfaces* **2019**, *11*, 18404; b) M. R. Laskar, D. H. K. Jackson, S. Xu, R. J. Hamers,

© 2021 The Authors. Advanced Functional Materials published by Wiley-VCH GmbH

D. Morgan, T. F. Kuech, *ACS Appl. Mater. Interfaces* **2017**, *9*, 11231.

[14] a) A. Aboulaich, K. Ouzaouit, H. Faqir, A. Kaddami, I. Benzakour, I. Akalay, *Mater. Res. Bull.* **2016**, *73*, 362; b) H. G. Song, S. B. Kim, Y. J. Park, *J. Electroceram.* **2012**, *29*, 163.

[15] a) Y. Wu, H. Ming, M. Li, J. Zhang, W. Wahyudi, L. Xie, X. He, J. Wang, Y. Wu, J. Ming, *ACS Energy Lett.* **2019**, *4*, 656; b) Z. Chen, G.-T. Kim, Y. Guang, D. Bresser, T. Diemant, Y. Huang, M. Copley, R. J. Behm, S. Passerini, Z. Shen, *J. Power Sources* **2018**, *402*, 263; c) Y. Kim, J. Cho, *J. Electrochem. Soc.* **2007**, *154*, A495.

[16] a) Q. Gan, N. Qin, Y. Zhu, Z. Huang, F. Zhang, S. Gu, J. Xie, K. Zhang, L. Lu, Z. Lu, *ACS Appl. Mater. Interfaces* **2019**, *11*, 12594; b) Y. Cao, X. Qi, K. Hu, Y. Wang, Z. Gan, Y. Li, G. Hu, Z. Peng, K. Du, *ACS Appl. Mater. Interfaces* **2018**, *10*, 18270; c) G.-L. Xu, Q. Liu, K. K. S. Lau, Y. Liu, X. Liu, H. Gao, X. Zhou, M. Zhuang, Y. Ren, J. Li, M. Shao, M. Ouyang, F. Pan, Z. Chen, K. Amine, G. Chen, *Nat. Energy* **2019**, *4*, 484.

[17] L. Liang, W. Zhang, F. Zhao, D. K. Denis, F. u. Zaman, L. Hou, C. Yuan, *Adv. Mater. Interfaces* **2020**, *7*, 1901749.

[18] A. J. Naylor, E. Makkos, J. Maibach, N. Guerrini, A. Sobkowiak, E. Björklund, J. G. Lozano, A. S. Menon, R. Younesi, M. R. Roberts, K. Edström, M. S. Islam, P. G. Bruce, *J. Mater. Chem. A* **2019**, *7*, 25355.

[19] A. Mansour, *Surf. Sci. Spectra* **1994**, *3*, 279.

[20] a) D. H. Cho, C. H. Jo, W. Cho, Y. J. Kim, H. Yashiro, Y. K. Sun, S. T. Myung, *J. Electrochem. Soc.* **2014**, *161*, A920; b) Z. Chen, Z. Wang, G.-T. Kim, G. Yang, H. Wang, X. Wang, Y. Huang, S. Passerini, Z. Shen, *ACS Appl. Mater. Interfaces* **2019**, *11*, 26994; c) C.-H. Jo, D.-H. Cho, H.-J. Noh, H. Yashiro, Y.-K. Sun, S. T. Myung, *Nano Res.* **2015**, *8*, 1464.

[21] a) S. Doubaji, B. Philippe, I. Saadoune, M. Gorgoi, T. Gustafsson, A. Solhy, M. Valvo, H. Rensmo, K. Edström, *ChemSusChem* **2016**, *9*, 97; b) G. Beamson, *The Scienta ESCA 300 Database*, **1992**.

[22] R. Tatara, P. Karayaylali, Y. Yu, Y. Zhang, L. Giordano, F. Maglia, R. Jung, J. P. Schmidt, I. Lund, Y. Shao-Horn, *J. Electrochem. Soc.* **2019**, *166*, A5090.

[23] a) R. Crowe, J. P. S. Badyal, *J. Chem. Soc., Chem. Commun.* **1991**, 958; b) M. A. Muñoz-Márquez, M. Zarrabeitia, E. Castillo-Martínez, A. Eguía-Barrio, T. f. Rojo, M. Casas-Cabanas, *ACS Appl. Mater. Interfaces* **2015**, *7*, 7801.

[24] a) X. Ding, Y.-X. Li, F. Chen, X.-D. He, A. Yasmin, Q. Hu, Z.-Y. Wen, C.-H. Chen, *J. Mater. Chem. A* **2019**, *7*, 11513; b) O. Tiurin, N. Solomatin, M. Auinat, Y. Ein-Eli, *J. Power Sources* **2020**, *448*, 227373; c) S. J. Shi, J. P. Tu, Y. Y. Tang, Y. Q. Zhang, X. Y. Liu, X. L. Wang, C. D. Gu, *J. Power Sources* **2013**, *225*, 338.

[25] a) K.-J. Park, J.-Y. Hwang, H.-H. Ryu, F. Maglia, S.-J. Kim, P. Lamp, C. S. Yoon, Y.-K. Sun, *ACS Energy Lett.* **2019**, *4*, 1394; b) W. Xue, M. Huang, Y. Li, Y. G. Zhu, R. Gao, X. Xiao, W. Zhang, S. Li, G. Xu, Y. Yu, *Nat. Energy* **2021**, *6*, 495.

[26] a) J. Kalhoff, G. G. Eshetu, D. Bresser, S. Passerini, *ChemSusChem* **2015**, *8*, 2154; b) I. H. Son, J. H. Park, S. Park, K. Park, S. Han, J. Shin, S.-G. Doo, Y. Hwang, H. Chang, J. W. Choi, *Nat. Commun.* **2017**, *8*, 1561.

[27] Z. Chen, X. Gong, H. Zhu, K. Cao, Q. Liu, J. Liu, L. Li, J. Duan, *Front. Chem.* **2019**, *6*, 643.

[28] a) H. Kim, J. Jang, D. Byun, H.-S. Kim, W. Choi, *ChemSusChem* **2019**, *12*, 5253; b) Y. Cho, P. Oh, J. Cho, *Nano Lett.* **2013**, *13*, 1145.

[29] a) Q. Wu, S. Mao, Z. Wang, Y. Tong, Y. Lu, *Nano Select* **2020**, *1*, 111; b) A. Nurpeissova, D.-I. Park, S.-S. Kim, Y.-K. Sun, *J. Electrochem. Soc.* **2015**, *163*, A171; c) A. Andersson, D. Abraham, R. Haasch, S. MacLaren, J. Liu, K. Amine, *J. Electrochem. Soc.* **2002**, *149*, A1358.

[30] a) J. Gnanaraj, E. Zinigrad, L. Asraf, H. Gottlieb, M. Sprecher, M. Schmidt, W. Geissler, D. Aurbach, *J. Electrochem. Soc.* **2003**, *150*, A1533; b) J. Yang, Y. Xia, *J. Electrochem. Soc.* **2016**, *163*, A2665.

[31] a) Y. Zhang, Y. Katayama, R. Tatara, L. Giordano, Y. Yu, D. Fraggedakis, J. G. Sun, F. Maglia, R. Jung, M. Z. Bazant, Y. Shao-Horn, *Energy Environ. Sci.* **2020**, *13*, 183; b) Y. Yu, P. Karayaylali, Y. Katayama, L. Giordano, M. Gauthier, F. Maglia, R. Jung, I. Lund, Y. Shao-Horn, *J. Phys. Chem. C* **2018**, *122*, 27368.

[32] a) L. Assumma, C. Iojoiu, R. Mercier, S. Lyonnard, H. D. Nguyen, E. Planes, *J. Polym. Sci., Part A: Polym. Chem.* **2015**, *53*, 1941; b) H.-D. Nguyen, G.-T. Kim, J. Shi, E. Paillard, P. Judeinstein, S. Lyonnard, D. Bresser, C. Iojoiu, *Energy Environ. Sci.* **2018**, *11*, 3298.

© 2021 The Authors. Advanced Functional Materials published by Wiley-VCH GmbH